1 **Accounting for Changes in Radiation Improves the Ability of SIF to Track Water**
2 **Stress-Induced Losses in Summer GPP in a Temperate Deciduous Forest**

3

4 **Zachary Butterfield[1], Troy Magney[2], Katja Grossmann[3], Gil Bohrer[4], Chris Vogel[5],**
5 **Stephen Barr[1], Gretchen Keppel-Aleks[1]**

6 [1]Climate and Space Sciences and Engineering, University of Michigan, Ann Arbor, Michigan.

7 [2]Department of Plant Sciences, University of California, Davis, California.

8 [3]Institute of Environmental Physics, University of Heidelberg, Heidelberg, Germany.

9 [4]Civil, Environmental and Geodetic Engineering, Ohio State University, Columbus, Ohio.

10 [5]University of Michigan Biological Station, Pellston, Michigan.

11

12 Corresponding author: Zachary Butterfield (zbutterf@umich.edu)

13

14 **Key Points:**

15 • Solar-induced chlorophyll fluorescence above a temperate deciduous forest is more
16   strongly tied to radiation than to productivity.

17 • Relative solar-induced fluorescence signals provide the strongest proxy for water stress-
18   induced summer losses in productivity.

19 • The ratio of red to far-red solar-induced fluorescence is sensitive to phenological changes
20   in canopy structure and downwelling radiation.

Abstract

As global observations of solar-induced chlorophyll fluorescence (SIF) have become available from multiple satellite platforms, SIF is increasingly used as a proxy for photosynthetic activity and ecosystem productivity. Because the relationship between SIF and gross primary productivity (GPP) depends on a variety of factors including ecosystem type and environmental conditions, it is necessary to study SIF observations across various spatiotemporal scales and ecosystems. To explore how SIF signals relate to productivity over a temperate deciduous forest, we deployed a PhotoSpec spectrometer system at the University of Michigan Biological Station AmeriFlux site (US-UMB) in the northern Lower Peninsula of Michigan during the 2018 and 2019 growing seasons. The PhotoSpec system consisted of two narrowband spectrometers, for the retrieval of SIF in the red (680-686 nm) and far-red (745-758 nm) regions of the electromagnetic spectrum, and a broadband spectrometer for the assessment of vegetation indices. We found that SIF correlated with GPP across diurnal and seasonal cycles, but that SIF irradiances were more strongly related to downwelling radiation than GPP. However, while this dependence of SIF on radiation obscured drought signals in SIF itself, we demonstrate that a SIF response to severe drought was apparent as a decrease in relative SIF. These results highlight the potential of SIF for detecting stress-induced losses in forest productivity. Additionally, we found that the red:far-red SIF ratio did not exhibit a response to drought stress, but was largely driven by seasonal and interannual changes in canopy structure, as well as by synoptic changes in downwelling radiation.

Plain Language Summary

Satellite measurements of solar-induced chlorophyll fluorescence (SIF), a faint light signal emitted from vegetation during photosynthesis, are increasingly being used to estimate ecosystem productivity and carbon uptake. To accurately do so requires a robust understanding of how the relationship between SIF and plant productivity changes over time, in response to environmental stressors, and across different ecosystems. To better understand SIF signals and how they relate to carbon uptake over a temperate deciduous forest, we used a high-precision spectrometer system to observe SIF signals at an AmeriFlux site (US-UMB) in the northern Lower Peninsula of Michigan. While the shared dependence of SIF and ecosystem productivity on sunlight lead to strong daily and seasonal correlations, we found that SIF signals were more closely tied to the amount of incoming sunlight than to ecosystem productivity. Despite the stronger dependence of SIF on sunlight, we show that drought conditions lead to a lower SIF relative to the total light signal. Lastly, we show that the observation of SIF at multiple wavelengths may provide additional information on seasonal and interannual changes in canopy structure. Our results demonstrate the value and limitations in using SIF to assess carbon dynamics over temperate deciduous forest ecosystems.

1 Introduction

Global ecosystems currently provide a sink for roughly one quarter of anthropogenic carbon emissions (Friedlingstein et al., 2022), and the climate-driven variations in this carbon sink therefore have significant implications for long-term changes in climate. Direct quantification of net and gross ecosystem productivity at regional to global scales is elusive, however, given the spatial heterogeneity of the global land surface and the sparse nature of direct observations of land-atmosphere carbon exchange, and contributes significant uncertainty to the global carbon budget (Friedlingstein et al., 2022; le Quéré et al., 2018).

65   The unique challenges involved in quantifying the biospheric carbon sink at the global
66   scale underscore the need for satellite-based observations that allow for the inference of
67   ecosystem productivity across a variety of ecosystems and spatiotemporal scales. Traditionally,
68   optical indices such as the normalized difference vegetation index (NDVI) have been used to
69   quantify ecosystem productivity (Tucker, 1979). These signals represent the 'greenness' of
70   vegetation which relates to the amount of light absorbed by vegetation, and empirically correlate
71   with productivity across spatial gradients. However, vegetation indices lack a direct mechanistic
72   relation with the short-term variations of photosynthetic rates, and thus require ancillary
73   meteorological data to account for environmental stressors and to estimate light use efficiency
74   (LUE), which is the efficiency at which sunlight is used to drive photochemistry and carbon
75   fixation (Running et al., 2004). Additionally, vegetation indices can be vulnerable to saturation
76   effects (X. Yang et al., 2015) or influenced by factors unrelated to vegetation, such as snow
77   cover (Beck et al., 2006).

78   Solar-induced chlorophyll fluorescence (SIF) is a newer space-based proxy for terrestrial
79   photosynthesis (Frankenberg, Butz, et al., 2011). As leaves absorb solar photons for use in
80   photosynthesis, photons not used for photochemistry are either dissipated as heat via non-
81   photochemical quenching (NPQ) or are fluoresced back to the environment as SIF. SIF,
82   therefore, is directly related to activity of the photosynthetic machinery, as it represents an
83   emission of red and far-red photons from the photosystems. Satellite observations of far-red SIF
84   have been shown to scale with spatial and seasonal patterns of gross primary productivity (GPP;
85   Frankenberg, Fisher, et al., 2011; Sun et al., 2017), indicating a potential for SIF as a direct
86   proxy of carbon uptake through photosynthesis. There has been a recent proliferation of satellite-
87   based observations of far-red SIF (Frankenberg et al., 2014; Joiner et al., 2013; Köhler et al.,
88   2018) and, more recently, red SIF (Köhler et al., 2020; Wolanin et al., 2015). Quantitative
89   assessments of SIF signals across a range of ecosystems and spatial and temporal scales are
90   needed to inform the interpretation of these data.

91   The strong relationship between SIF and GPP stems in part from a shared dependence on
92   solar radiation (Magney et al., 2020). Top-of-canopy SIF can be expressed as:

93    $$SIF = PAR \times fPAR \times SIF_{yield} \times f_{esc} \qquad (1)$$

94   (Zeng et al., 2019) where fluorescence yield (SIF_{yield}) represents the efficiency at which the
95   photosystems emit photons, photosynthetically active radiation (PAR) indicates downwelling
96   radiation available for photosynthesis, and fPAR indicates the fraction of PAR absorbed by the
97   canopy, which depends primarily on green leaf area, chlorophyll content, and canopy structure.
98   The fluorescence escape ratio (f_{esc}) represents the fraction of total emitted fluorescence that
99   escapes the top of canopy and can be detected remotely, rather than being deflected or
100   reabsorbed by leaves deeper within the canopy (Dechant et al., 2020; Zeng et al., 2019).
101   Similarly, GPP can be expressed as the product of PAR, fPAR, and LUE (X. Yang et al., 2015):

102   $$GPP = PAR \times fPAR \times LUE \qquad (2)$$

103   As LUE is the most difficult component of GPP to estimate using remote sensing and is
104   traditionally inferred from models (Gitelson & Gamon, 2015; Monteith, 1977), there is much
105   interest in characterizing its relationship with SIF (and SIF_{yield}, or the rate at which absorbed
106   photons are fluoresced as SIF). X. Yang et al. (2015) showed that SIF contained some
107   information about LUE over a temperate deciduous forest, by dividing tower-based SIF by total

108 absorbed PAR to reveal a weak correlation between LUE and SIF_{yield}, although this relationship
109 was weaker than the correlation between far-red SIF and GPP.

110   Magney, Bowling, et al. (2019) and Pierrat et al. (2022) further showed a strong
111 relationship between SIF and GPP in northern evergreen forests under minimal changes in
112 canopy structure and absorbed PAR, when more traditional observations such as NDVI, which
113 are closely tied to changes in chlorophyll content, did not capture seasonal productivity
114 dynamics. The demonstrated seasonality in SIF, even when greenness remains constant, suggests
115 that the SIF signal is sensitive to seasonal changes in photoprotective pigments and LUE, and
116 therefore provides a more robust proxy of GPP than greenness alone.

117   Despite the strong correlations reported between SIF and GPP at seasonal and diurnal
118 timescales, uncertainties remain in the mechanistic relationship between SIF and GPP (Ryu et
119 al., 2019), and in how that relationship changes across different ecosystems and spatiotemporal
120 scales. Several studies have found that SIF over cropland is more closely tied to absorbed PAR
121 (APAR) than to GPP (Miao et al., 2018; K. Yang et al., 2018; Yazbeck et al., 2021), and Zeng et
122 al. (2019) broadly demonstrated that SIF is strongly influenced by canopy structure and changes
123 in f_{esc}. SIF is also dependent on the fluorescence yield of the photosystems. Furthermore, while
124 GPP is sensitive to ecosystem stress through changes in LUE, it is not understood how
125 fluorescence yield, and therefore observed SIF, responds to stress-induced changes. It is
126 therefore unclear how closely the SIF response to environmental stressors mirrors changes in
127 GPP. Several satellite-based studies have used SIF to observe the impacts of moderate to severe
128 drought (Li et al., 2020; Song et al., 2018; Yoshida et al., 2015); nonetheless, observations of SIF
129 tend to be less sensitive to interannual variability in GPP during summer and may not show the
130 impacts of mild stress (Butterfield et al., 2020). Furthermore, Yazbeck et al. (2021) demonstrated
131 that SIF did not reliably capture daily-scale reductions in GPP due to water stress at multiple flux
132 tower sites. Wohlfahrt et al. (2018) showed that local scale observations of SIF over a
133 Mediterranean pine forest decoupled from GPP under environmental stress and suggested that
134 much of the strong correlation between SIF and GPP in this ecosystem was driven by a shared
135 dependence on APAR, calling into question the detectability of stress-induced changes in GPP
136 from SIF observations. However, they also noted an increase in the red:far-red SIF ratio aligning
137 with peak stress conditions. The differing behaviors of red and far-red SIF signals during an
138 ecosystem stress event warrant further investigations into what can be learned from simultaneous
139 observations of SIF at both red and far-red wavelengths.

140   To assess the relationship between SIF and GPP and their responses to environmental
141 variables and stressors, we deployed a tower-based PhotoSpec spectrometer system (Grossmann
142 et al., 2018) above a temperate deciduous forest within the footprint of the US-UMB flux tower
143 at the University of Michigan Biological Station. We present results from two years of growing-
144 season observations, during which we collected red and far-red SIF observations at a high
145 temporal frequency (~20 s), providing an opportunity to quantify diurnal and intraseasonal
146 variation in the SIF signal. Our goals were to: 1) explore the dependence of SIF on downwelling
147 PAR and test how this dependence influenced the ability of SIF to track intraseasonal changes in
148 GPP; 2) characterize the relationship between SIF and GPP and test how it changed over the
149 course of the growing season and during periods of water stress; and 3) explore the behavior of
150 the red:far-red SIF ratio and assess its response to changes in environmental conditions.

151 **2 Data and Methods**

152   2.1 Study Location at University of Michigan Biological Station

153   We obtained data at the University of Michigan Biological Station site within a
154 deciduous broadleaf forest composed primarily of aspen, oak, maple, beech, and some
155 understory pine, with a canopy height of approximately 22 m. The forest age is roughly one
156 century as widespread fires burned much of the region in the early twentieth century. The site is
157 characterized by sandy soil, with rapid percolation of rainfall to deep soil layers. This location
158 was chosen in part because it is a well-studied forest ecosystem, with long-standing eddy
159 covariance-based observations of water and carbon fluxes (Frasson et al., 2015; Gough et al.,
160 2013, 2022), canopy structure (Fotis et al., 2018), soil moisture (He et al., 2014), and sap flow
161 and tree hydrology (Aron et al., 2019; Matheny et al., 2014, 2017).

162   2.2 PhotoSpec Tower-Based Observations

163   We built and deployed a PhotoSpec spectrometer system (Grossmann et al., 2018) at the
164 US-UMB tower during the 2018 and 2019 growing seasons (Butterfield et al., 2022). The
165 PhotoSpec system consisted of two narrowband spectrometers (QEPro, Ocean Optics Inc.): one
166 with a wavelength range of 670-732 nm and a resolution of 0.074 nm/pixel, 0.3 nm full width
167 half maximum (FWHM), for measuring SIF in the red region of the spectrum, and a second
168 QEPro (729-784 nm, 0.067 nm/pixel, 0.3 nm FWHM) optimized for measuring SIF in the far-
169 red. An additional broadband spectrometer (Flame, Ocean Optics Inc.; 177-874 nm, 0.382
170 nm/pixel, 1.2 nm FWHM) permitted the calculation of vegetation indices, such as NDVI, from
171 the measured spectra. A 2-D scanning telescope was mounted on the US-UMB tower at a height
172 of 45 m and could point at various locations in the canopy using a narrow field of view (about
173 0.7°). Light from the canopy was thus directed through a fiber optic cable, and subsequently
174 split as input to the three spectrometers.

175   We acquired automated observations in three azimuthal directions: 60° east of south, due
176 south, and 60° west of south. For each azimuth angle, we acquired data along an elevation
177 transect by scanning from 90° (nadir) to 45° below the horizon. For each individual location
178 along the transects, we optimized the exposure times for the spectrometers to maintain consistent
179 detector signal level. Multiple exposures were then integrated together into 20 s measurements
180 before moving the telescope to the next location. Observations were collected when the solar
181 elevation angle was > 10° and solar reference spectra were collected at least every 10
182 measurements using an upward-facing diffuser disk. To ensure that observations included green
183 vegetation and were of sufficiently high quality, data were further filtered to only include
184 retrievals where NDVI was > 0.2, red and far-red SIF retrieval errors were < 0.1 mW m^{-2} sr^{-1}
185 nm^{-1}, and SIF irradiances were calculated to be between -0.1 and 10 mW m^{-2} sr^{-1} nm^{-1} and
186 between -2 and 20% of the total light signal. These filters resulted in the removal of ~12% of
187 collected data. A full cycle through the three azimuth angles took approximately 90 minutes;
188 therefore, after removing outlier data, we used 90-minute averages for sub-daily comparisons.

189   The uncertainty of each 90-minute period was calculated as the standard deviation of included
190   observations.

191   SIF irradiances were calculated from the QEPro spectra for both the red (680-686 nm)
192   and far-red (745-758 nm) regions of the electromagnetic spectrum using a physical retrieval
193   based on the infilling of solar Fraunhofer lines (Grossmann et al., 2018). To isolate SIF signals
194   from their dependence on PAR, we calculated relative SIF by dividing the observed SIF
195   irradiance by the total reflected and fluoresced irradiance at the respective wavelength to
196   represent SIF as a percentage of the total light signal. We calculated NDVI, the photochemical
197   reflectance index (PRI), which is sensitive to de-epoxidation of xanthophyll cycle pigments and
198   light use efficiency (Gamon et al., 2001), and a chlorophyll index (Chlorophyll$_{RS}$; Magney,
199   Frankenberg, et al., 2019; Datt, 1999) using spectra from the broadband Flame spectrometer
200   (Text S1). While our site did not include direct observations of fPAR, we assume a rough
201   proportionality between NDVI and fPAR (Running et al., 2004) from which we inferred the
202   qualitative seasonal behavior of fPAR (i.e., we assumed that seasonal changes in fPAR tracked
203   seasonal changes in NDVI).

204   The SIF observations were radiometrically calibrated using a second broadband Flame
205   spectrometer with a cosine corrector (CC-3-UV-S, Ocean Optics Inc.) that was calibrated using
206   radiometric standard lamp (HL-3-P-CAL, Ocean Optics Inc.). We recorded simultaneous
207   measurements alongside the PhotoSpec instrument with the second Flame spectrometer using a
208   reflective calibration disk (Spectralon Diffuse Reflectance Standard, Labsphere Inc.) at least
209   once per growing season whenever any adjustments were made to the optical components.
210   Between the 2018 and 2019 growing seasons, radiometric calibration coefficients remained
211   within 2.5 and 1% for red and far-red SIF retrievals, respectively. Wavelength calibrations were
212   done using a Mercury-Argon lamp (HG-1, Ocean Optics Inc.).

213   2.3 AmeriFlux and Meteorological Data

214   For this study, we compared PhotoSpec SIF data with ecosystem flux observations from
215   the AmeriFlux tower (46 m above ground), from which CO_2 and H_2O flux data have been
216   observed since 1999 (Gough et al., 2022). Eddy covariance (EC) flux observations of Net
217   Ecosytem Exchange (NEE) were partitioned into estimates of ecosystem respiration (RE) and
218   GPP, from which we used the processed half-hourly estimates of GPP from April 2018 through
219   November 2019. We used the data from 2007-2019 for a baseline comparison with a multi-year
220   mean. In addition to GPP flux data, we used coincident meteorological observations from the
221   same AmeriFlux dataset. These included air temperature, precipitation, vapor pressure deficit
222   (VPD), volumetric soil water content (SWC) at a depth of 30 cm, and downwelling PAR. Data
223   for the site was obtained through the AmeriFlux database (AmeriFlux site ID: US-UMB; Gough
224   et al., 2022). More details about the data processing approach for this site are described by
225   Gough et al. (2013).

226   Flux data were processed by the site team following the standard EC processing protocol
227   (Rebmann et al., 2012). Flux data during periods of low turbulent mixing were filtered using the
228   u*-filter threshold approach, with the threshold values calculated seasonally following
229   Reichstein et al. (2005). Filtered nighttime NEE observations were assumed to represent RE, and
230   seasonal nighttime RE observations were then used to train an automated neural network model

231 (ANN; see Morin et al., 2014) to infer daytime RE using time of day, air temperature, vapor
232 pressure deficit, soil temperature, and soil moisture as inputs (Lasslop et al., 2010). For all ANN
233 models, 50% of the data were used for training, 25% for evaluation and 25% for validation of the
234 ensemble's goodness of fit. The ensemble mean of the best-performing 10% of 1000 ANN
235 models was used to predict RE during the day, and during nighttime observation gaps. GPP was
236 assumed to be zero during winters and overnight, and daytime GPP during the growing season
237 was calculated as the difference between observed NEE and modelled RE. ANN models with a
238 setup similar to the one used for RE were used to model GPP and gapfill missing daytime
239 observations during the growing season. The GPP ANN models used air temperature, incoming
240 PAR, relative humidity, vapor pressure deficit, sensible and latent heat fluxes, and soil moisture
241 as input variables.

242 We aggregated the half-hourly AmeriFlux data to 90-minute and daily values for each
243 variable either by simple summation (precipitation) or averaging (other variables). As NDVI
244 (and therefore fPAR) was generally constant between leaf out and senescence, we calculated an
245 LUE proxy as GPP/PAR (Gitelson & Gamon, 2015). Seasonal estimates for species-specific
246 maximal leaf area index (LAI) at the site were measured using samples collected with leaf litter
247 traps.

248 2.4 Satellite Observations of SIF from OCO-2

249 We compared satellite-based observations of SIF from the Orbiting Carbon
250 Observatory-2 (OCO-2; Science Team et al., 2017; Yu et al., 2019) with our tower-based
251 PhotoSpec observations. OCO-2 is a polar orbiting satellite with a local overpass time of
252 1:30pm. SIF was retrieved from OCO-2 spectra at 757 nm and 771 nm using a non-linear least-
253 squares approach to evaluate the infilling of solar Fraunhofer lines (Sun et al., 2018). We
254 averaged OCO-2 SIF retrievals at 757 nm (which was within our far-red fitting window of 745-
255 758 nm) that fell within a one-degree grid cell centered at US-UMB. Individual soundings were
256 converted to daily-averages using a clear-sky PAR proxy, which uses the cosine of the solar
257 zenith angle to account for diurnal variability in the SIF signal. We subsequently calculated a
258 single mean and standard deviation of OCO-2 observations for each day with available overpass
259 data, resulting in nine individual data points throughout the 2018 and 2019 growing seasons. We
260 then tested the linear correlation of these data with corresponding daily means observed using the
261 PhotoSpec instrument.

3 Results

263 3.1 Climatological Context for 2018-2019 Growing Seasons

264 The 2018 and 2019 growing seasons were both more productive than the 2007-2019
265 mean based on eddy covariance GPP data (Figure 1a). In 2018, growing season onset was
266 delayed by about a week relative to the multi-year mean, but GPP increased rapidly (~0.5 µmol
267 m^{-2} s^{-1} day^{-1}) throughout the second half of May during a period with above average
268 temperatures (Figure 1a-b). GPP reached a seasonal peak value of about 10 µmol m^{-2} s^{-1} in late
269 June, roughly 25% higher than the multi-year mean, and remained higher than average until mid-
270 August. In 2019, onset of the growing season occurred even later, following the multi-year mean
271 by about 2 weeks, due to very wet and cold spring conditions (Figure 1b-c). GPP subsequently

272 reached a peak value of > 12 µmol m^{-2} s^{-1} day^{-1} in late July, 50% higher than the multi-year
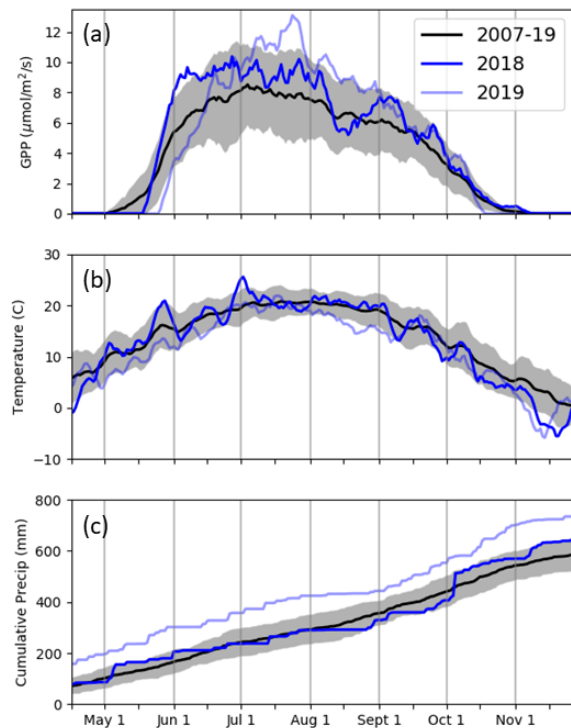273 mean, and remained nearly a standard deviation higher than average until September (Figure 1a).

274
275 **Figure 1**. Observations of GPP (a), temperature (b), and cumulative precipitation (c) at US-UMB during
276 the 2018 (dark blue) and 2019 (light blue) growing seasons. The 2007-2019 multi-year mean for each
277 panel is included as a black line, with shading representing ±1 standard deviation. GPP and temperature
278 are plotted as 7-day running means.

279   Both 2018 and 2019 experienced water stress-induced declines in GPP during late
280 summer that occurred with moderate to severe drought conditions as classified by the U. S.
281 Drought Monitor (USDM; Svoboda et al., 2002; accessed via http://droughtmonitor.unl.edu).
282 The USDM classification showed a severe drought in mid-August 2018 that followed a series of
283 three dry spells in early June, early July, and August (Figure 1c). While the first of these dry
284 periods did not lead to dry soil moisture conditions, the cumulative influence of the two later dry
285 periods led to soil water content falling to ~5% and coincided with local maxima in VPD
286 upwards of 9 hPa (Figure 2g). GPP levels were relatively robust during the first period of dry
287 soil conditions from late June through July 11, but during the second dry period from late July
288 through August 18, productivity ultimately declined by about 30%, to levels below the multi-
289 year mean. Towards the end of August, GPP recovered back to about 20% above the
290 climatological mean. GPP may be increasingly sensitive to dry soil conditions over the growing
291 season due to the fact that the soil matric potential can continue to increase even as SWC
292 asymptotes to a lower limit (Köcher et al., 2009; Lascano et al., 2007). The soil matric potential
293 reflects soil hydraulic tension, which at higher values indicates greater resistance to vegetation
294 taking up water through their roots. Late summer declines in GPP occur roughly every other year
295 at the US-UMB site and are not always tied to an obvious drought signal (Figure S1). While
296 2019 was not characterized by any periods of severe drought stress, GPP observations did

297 decrease in late July from about 50% to only 20% above the climatological mean (Figure 1a).
298 This decline in productivity coincided with decreasing SWC (Figure 2h) and little accumulated
299 precipitation (Figure 1c), but also with cooler temperatures (Figure 1b) and only a slight increase
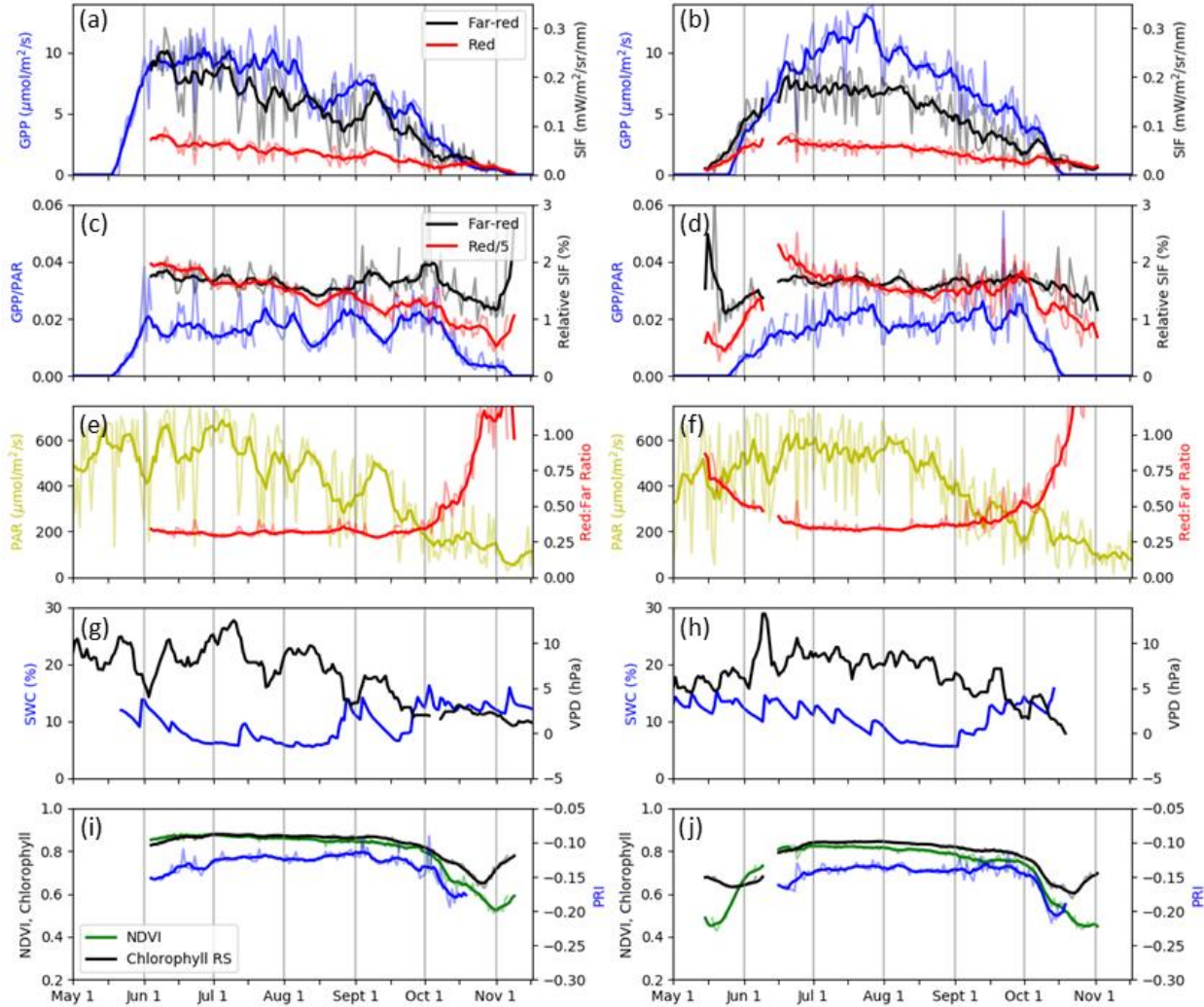300 in VPD (Figure 2h).

301
302 **Figure 2**. Growing season time series of GPP and SIF irradiance (a, b), GPP/PAR and relative SIF (c, d),
303 photosynthetically active radiation (PAR) and the red:far-red SIF ratio (e, f), soil water content (SWC)
304 and vapor pressure deficit (VPD (g, h), and NDVI, Chlorophyll$_{RS}$, and PRI (i, j) during 2018 (left) and
305 2019 (right). With the exception of SWC and VPD, bold lines represent the 7-day running mean of daily-
306 averaged data (thin lines).

307 3.2 Characteristics of Red and Far-red SIF Signals

308 Far-red SIF observations during 2018 and 2019 generally followed a seasonal cycle
309 similar to that of GPP (Figure 2a-b). Both SIF and GPP reached peak levels in early summer and
310 steadily declined throughout late summer and fall. The red SIF signal followed a similar pattern
311 but exhibited relatively higher values in early spring and fall (Figure 2a-b), illustrated by higher
312 red:far-red SIF ratios during the shoulder seasons (Figure 2e-f) corresponding with low NDVI
313 and Chlorophyll$_{RS}$ values (Figure 2i-j). This contrast between red and far-red SIF seasonality

314 results from top-of-canopy red SIF observations being more sensitive to canopy structure and
315 chlorophyll content (Magney, Frankenberg, et al., 2019), since a smaller fraction of total emitted
316 SIF is scattered or reabsorbed by the canopy during the springtime when the canopy is not yet
317 fully developed or as chlorophyll content decreases in fall. This dependence is also evident in
318 lower red:far-red SIF ratios in 2018, concurring with differences in other observations including
319 NDVI (maximum value of 0.88 in 2018 and 0.84 in 2019) and LAI, where measurements using
320 leaf litter traps showed almost a 20% reduction in 2019 compared to 2018 (4.38 in 2018 versus
321 3.64 in 2019; Table 1). The lower red:far-red SIF ratio in 2018, when LAI was high, corroborates
322 the hypothesis that a denser canopy limits top-of-canopy red fluorescence. Taken together, these
323 differences in the behavior of SIF at different wavelengths suggested that far-red SIF better
324 reflected the seasonal cycle of productivity in a temperate deciduous forest, and that red SIF was
325 more sensitive than far-red SIF to seasonal, and potentially interannual, changes in canopy
326 structure and chlorophyll concentration.

327

328 **Table 1**. Species-specific leaf area index (LAI) values as observed at the US-UMB AmeriFlux site for
329 2018 and 2019 using leaf litter traps.

330

Species	2018 LAI	2019 LAI
Bigtooth aspen (*Populus grandidentata*)	1.286	0.981
Red maple (*Acer rubrum*)	0.891	0.730
American beech (*Fagus grandifolia*)	0.292	0.281
Red oak (*Quercus rubra*)	1.073	0.878
Paper birch (*Betula papyrifera*)	0.238	0.178
White pine (*Pinus strobus*)	0.587	0.578
Red pine (Pinus resinosa)	0.008	0.011
Total	**4.375**	**3.636**

331 We calculated correlations between SIF and GPP with data aggregated to 90-minute,
332 daily, and weekly timescales (Figure 3). For far-red SIF, weekly-aggregated data had the highest
333 correlation with GPP ($R^2 = 0.81$), while 90-minute- and daily-aggregated data had R^2 values of
334 0.61 and 0.62, respectively. The correlations between GPP and red SIF were weaker (R^2 values

335   of 0.56, 0.54, and 0.72 for 90-minute, daily, and weekly timescales; Figure S2). Over the
336   growing season, weekly values of far-red SIF span the range from near zero during the early and
337   late growing season, to 0.2 mW m^{-2} sr^{-1} nm^{-1} during peak growing season in July (Figure 3d).
338   Daily values during the month of July, in contrast, have a standard deviation of ~0.05 mW m^{-2}
339   sr^{-1} nm^{-1} and reach as high as 0.3 mW m^{-2} sr^{-1} nm^{-1} (Figure 3c), suggesting that cloud-driven
340   variability in PAR may be a significant driver in far-red SIF variability while GPP in this
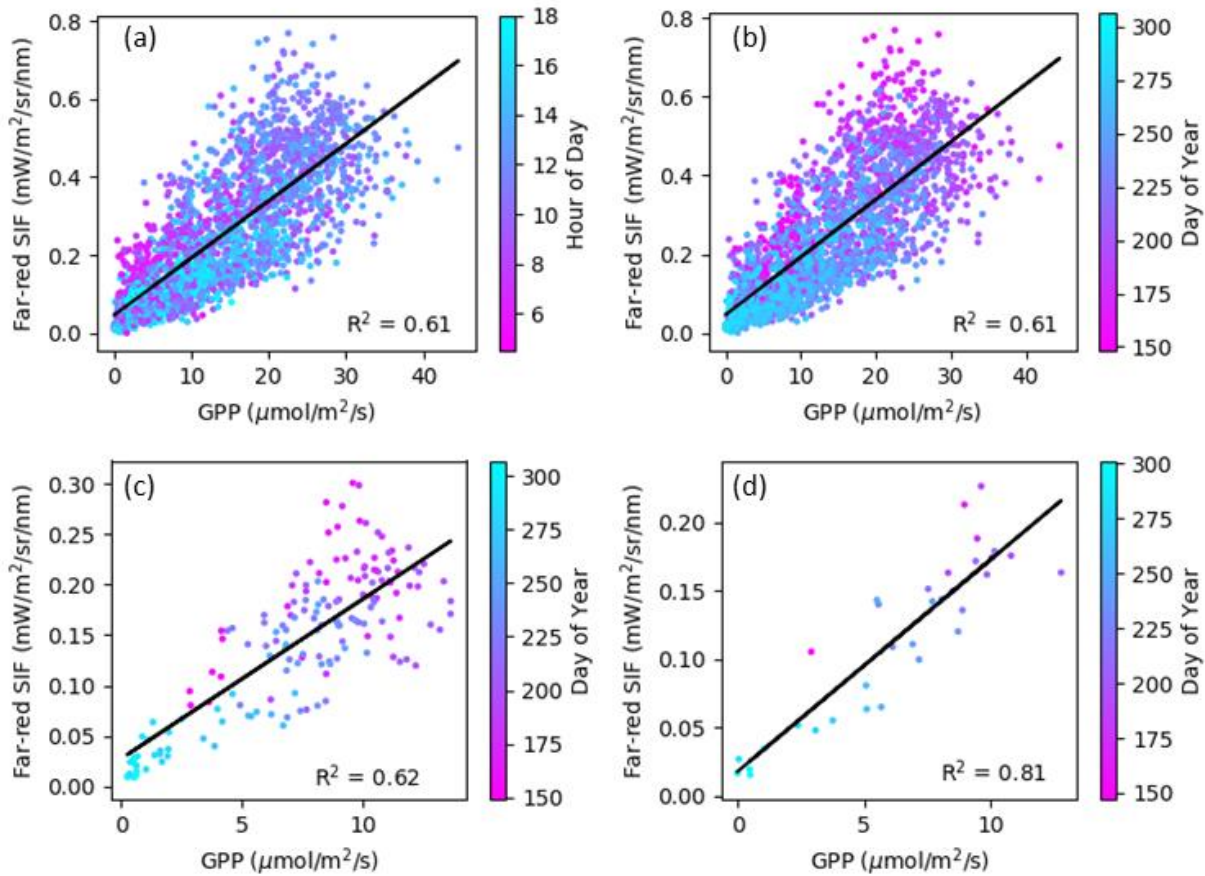341   ecosystem may be less sensitive to day-to-day variability in light availability.

342
343   **Figure 3**. Correlation between far-red SIF and GPP, temporally aggregated to 90-minute (a, b), daily (c),
344   and weekly (d) resolutions. Color bars indicate hour of day (a) or day of year (b-d).

345   To investigate how seasonal changes influence the relationship between GPP and far-red
346   SIF we fit linear correlations to data within individual months for 2018 and 2019 (Figure 4). We
347   quantified uncertainties both on slopes and R^2 values using a bootstrapping approach in which
348   we sampled the monthly data with replacement. Results for daily-averaged data confirmed that
349   GPP and far-red SIF are best correlated during spring and fall, when seasonal phenological
350   changes in the deciduous forest result in a large dynamic range in fPAR (using NDVI as a
351   proxy). Shared dependence on fPAR between SIF and GPP thus lead to stronger correlations
352   during these months (Figure 4d; discussed in more detail in section 4.1). Correlations between
353   90-minute data showed that the inclusion of diurnal variations led to consistently stronger
354   correlations throughout the summer (Figure 4b). The resulting slopes from the linear fits of daily
355   data exhibited large uncertainties and do not exhibit obvious changes over the course of the
356   growing season (Figure 4c). Linear fits of 90-minute data were better constrained to the origin by

357   including near-zero values in morning and evening, resulting in more precise slopes (Figure 4a).
358   These results showed that the far-red SIF:GPP slope was highest during the spring and declined
359   over the course of the growing season (Figure 4a; further discussed in Section 4.2).
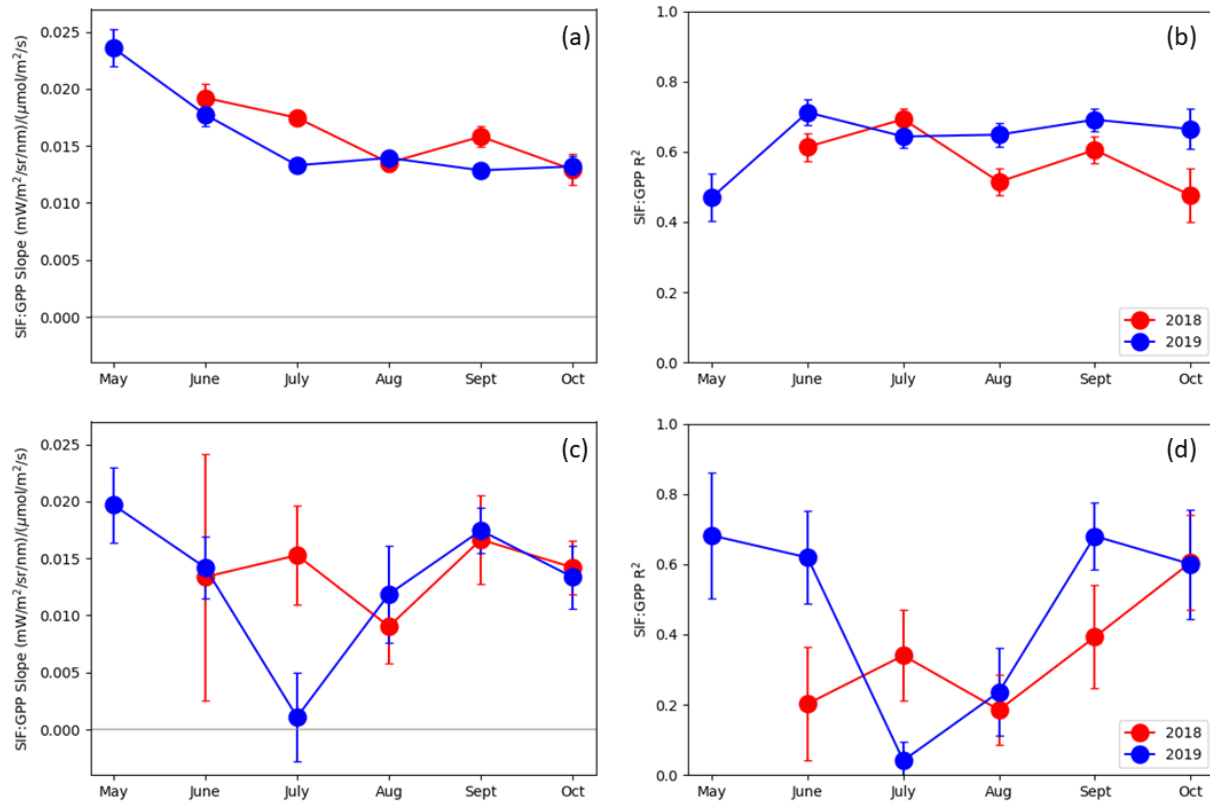

360
361   **Figure 4**. Slopes and R^2 values from monthly linear regressions of 90-minute- (a, b) and daily-averaged
362   (c, d) far-red SIF with GPP. Data from 2018 are in red, while 2019 data are in blue. Error bars represent
363   the standard deviations of results from a bootstrapping method used to test the robustness of the linear
364   regressions.

365   While both SIF and GPP depend on PAR (Equation 1 and 2), SIF was more tightly
366   coupled to downwelling PAR than was GPP at our site (Figure 5). Without direct observations of
367   fPAR, we assumed that fPAR was near constant under peak growing season conditions when
368   NDVI was stable (see Running et al., 2004; Figure 2i-j), and that the relationship during summer
369   between SIF and PAR were therefore indicative of the relationship between SIF and APAR. The
370   close dependence of SIF on radiation was illustrated by shared temporal patterns of SIF and PAR
371   throughout summer (Figure 2a-b, e-f), and by a strong correlation between daily-aggregated far-
372   red and red SIF with PAR ($R^2 = 0.90$, Figure 5a, S3). GPP and PAR exhibited a much weaker
373   correlation ($R^2 = 0.51$; Figure 5b). Monthly correlations of far-red SIF and GPP with PAR
374   confirmed that GPP exhibits a weaker relationship with downwelling PAR than SIF (Figure S4b,
375   d). Monthly correlations also showed that the relationship between SIF and PAR was weakest
376   during spring and fall (Figure S4d) when variations in NDVI (and fPAR), due to rapid changes
377   in the canopy (i.e. leaf-out and senescence), cause APAR to deviate qualitatively from PAR.
378   Lower NDVI (and fPAR) during spring and fall also led to lower values of SIF and GPP relative

379   to PAR (Figure S4a, c), as a smaller fraction of downwelling radiation is absorbed by vegetation
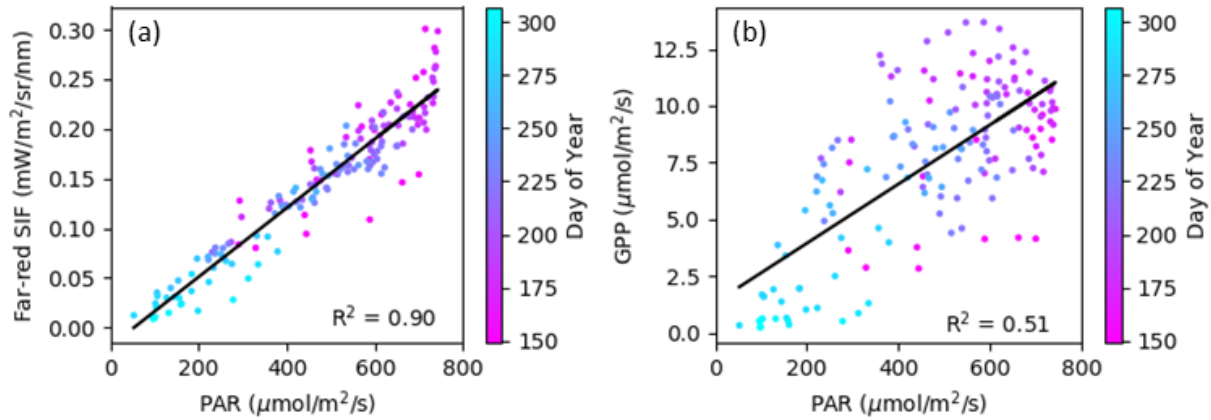380   during these periods.

381
382   **Figure 5**. Correlation between daily-averaged far-red SIF (a) and GPP (b) with photosynthetically active
383   radiation (PAR). Color bars are weighted by day of year.

384   We calculated relative SIF, or SIF as a fraction of the total light signal, in order to
385   decouple the SIF signal from its dependence on PAR (Figure 2c-d). During peak summer
386   conditions, relative far-red SIF typically was just under 2% of total observed light, while relative
387   red SIF was 5-10%. Red and far-red relative SIF exhibited lower values during early spring and
388   late fall, when the ecosystem absorbs less downwelling radiation for photosynthesis. We
389   calculated an LUE proxy as GPP divided by PAR and found that relative far-red and especially
390   red SIF visually track intraseasonal patterns in LUE (Figure 2c-d), notably during the August
391   2018 severe drought. Relative red SIF shares a similar seasonal pattern with GPP/PAR, leading
392   to a stronger correlation between daily-aggregated data ($R^2 = 0.34$; Figure S5b), while the
393   correlation between relative far-red SIF and GPP/PAR is weaker ($R^2 = 0.07$; Figure S5a).

394   3.3 Detectability of Mid-summer Ecosystem Stress

395   While there were clear stress-induced decreases in GPP inferred from eddy covariance in
396   August 2018 (Figure 2a; Section 3.1) coinciding with severe drought as classified by USDM
397   (Svoboda et al., 2002; accessed via http://droughtmonitor.unl.edu), these intraseasonal stress
398   dynamics were not obvious in remote sensing observations of SIF irradiances from PhotoSpec.
399   Variations in red and far-red SIF irradiances followed synoptic-scale patterns in downwelling
400   PAR (Figure 2a-b, e-f) rather than changes in GPP. Only relative red and far-red SIF values
401   showed a notable change coinciding with the mid-summer drought, which dipped to a local
402   minimum in mid-August (Figure 2c). Optical vegetation indices, including NDVI,
403   Chlorophyll$_{RS}$, and PRI, remained constant over the course of the growing season (Figure 2i-j),
404   indicating limited changes in chlorophyll and carotenoid pigments within the canopy.

405   To further investigate potential influences of drought stress on canopy SIF, we linearly
406   detrended peak growing season observations (between July 15 and September 15, 2018) to
407   distinguish intraseasonal variability from seasonal trends. We then calculated 5-day binned
408   averages of observed data over the course of the August 2018 drought (Figure 6), and calculated
409   correlation coefficients between detrended GPP and other variables over this period using both

410   daily and 5-day binned data (Table 2). GPP first experienced a decline around August 10 and
411   recovers roughly 20 days later, but the far-red and red SIF irradiances exhibited higher (instead
412   of lower) values over these 20 days (Figure 6a). The higher SIF irradiances during a cloud- and
413   precipitation-free period was consistent with the strong relationship with PAR demonstrated
414   above, however relative red and far-red SIF signals were more sensitive to ecosystem stress and
415   saw local minimum values during the second 5-day period of the drought (August 14-18; Figure
416   6b). Relative far-red SIF was the only variable to show a statistically significant ($p < 0.01$)
417   correlation with GPP at both daily and 5-day temporal scales, but did not exhibit significant
418   correlations with GPP/PAR, our LUE proxy, at daily ($R = -0.17$) or 5-day ($R = 0.08$) scales.
419   Relative red SIF, however, showed a strong correlation with GPP/PAR at both daily ($R = 0.69$)
420   and 5-day ($R = 0.87$) temporal scales. In contrast to Wohlfahrt et al. (2018), our observations did
421   not show a strong red:far-red SIF ratio response to drought-induced stress (Figure 6a, c;
422   discussed further in Section 4.3), but instead the detrended daily SIF ratio was strongly
423   anticorrelated ($R^2 = 0.79$) with PAR. Diurnal stress-induced effects were also not seen in the 90-
424   minute-aggregated observations of the red:far-red SIF ratio (Figure S6). We note that there was
425   a delayed increase in PRI following the drought by ~10 days (Figure 6), which may indicate an
426   increase in carotenoid pigments resulting from the drought period; however, we did not observe
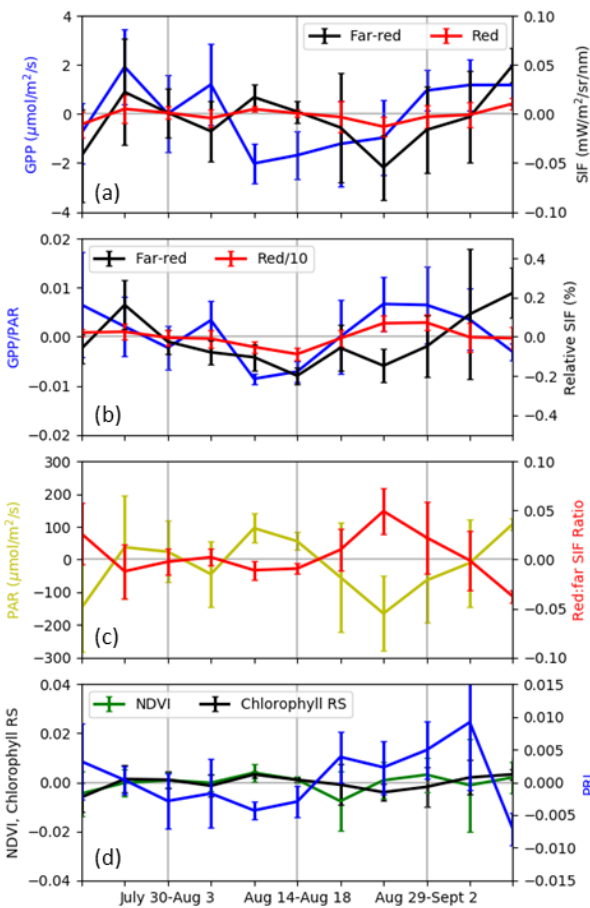427   any corresponding changes in Chlorophyll$_{RS}$ (Figure 6d).

Figure 6. Five-day binned and detrended data showing GPP and SIF irradiances (a), GPP/PAR and
relative SIF (b), the red:far-red SIF ratio and PAR (c), and NDVI, Chlorophyll$_{RS}$, and PRI (d) during
drought conditions in August 2018. Error bars represent the standard deviation of each five-day bin.

432 **Table 2**. R-values resulting from linear fits between detrended GPP and other variables between July 15
433 and September 15, 2018 for both daily and 5-day binned observations. Values in bold indicate statistically
434 significant fits ($p < 0.01$).
435

	Daily GPP	5-day binned GPP
Far-red SIF	**0.51**	0.31
Red SIF	**0.51**	0.29
Relative Far-red SIF	**0.56**	**0.76**
Relative Red SIF	0.20	0.43
Red:Far-red SIF Ratio	**-0.41**	-0.27
PAR	**0.39**	0.10
NDVI	0.15	0.12
Chlorophyll$_{RS}$	**0.37**	0.17
PRI	0.05	0.15

436   3.4 Comparison with Space-based SIF from OCO-2

437   The ultimate goal of our tower-based SIF observations is to improve the interpretation of
438 space-based, global SIF observations. We compared daily averages of far-red SIF observations
439 from PhotoSpec with mean estimates of daily-averaged SIF from the OCO-2 satellite (Figure 7).
440 The OCO-2 satellite observations were well correlated with our tower observations ($R^2 = 0.79$)
441 showing that both sets of observations captured proportionally similar patterns in the SIF signal.
442 However, the slope between the two datasets of 2.2 ± 0.4, reflected that the raw SIF irradiance
443 measured by OCO-2 was twice that measured by PhotoSpec. The lower irradiance values
444 observed by our PhotoSpec instrument likely resulted from including observations with larger
445 incident angles between solar and viewing directions, due to including elevation angles up to 45°
446 below horizon in the calculation of daily-averaged SIF, as well as deploying the telescope on the
447 south side of the tower. Thus, our tower-based observations included a greater fraction of shaded
448 vegetation because illumination and viewing angles were often from opposing cardinal
449 directions. These differences highlight that, while tower- and space-based platforms capture
450 similar relative patterns in SIF signals, more comprehensive comparisons between SIF
451 observations require a more complex study of viewing and illumination angle sensitivities in top-
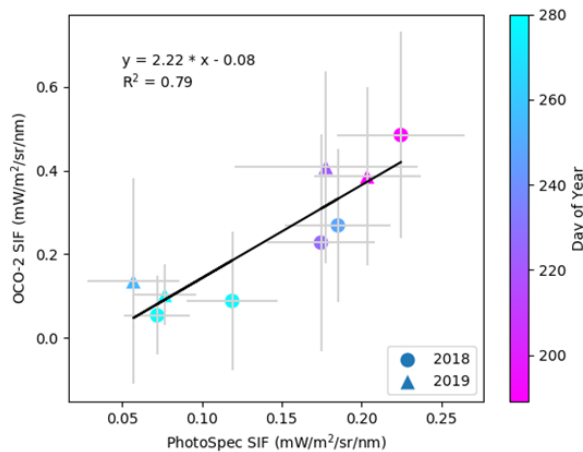452 of-canopy SIF observations.

453

454
455 **Figure 7**. Correlation plot and linear fit results between far-red SIF observations from PhotoSpec and the
456 OCO-2 satellite. OCO-2 data includes soundings within a one-degree gridcell centered at US-UMB. Each
457 sounding was multiplied by a daily correction factor, which uses a clear-sky proxy to account for diurnal
458 changes in the SIF signal. Means were calculated from soundings across individual days, and error bars
459 represent the standard deviation of included observations. Mean daily values from OCO-2 were then
460 correlated with the daily-average SIF signal seen from the PhotoSpec instrument, where uncertainties
461 were propagated from the standard deviation of 20 s observations included in every sub-daily 90-minute
462 average. Circles indicate data from 2018 and triangles indicate 2019. The color bar is weighted by day of
463 year.

464 **4 Discussion**

465   4.1 Dependence of SIF and GPP on PAR

466   While our results align with several studies that suggest that high correlations between
467 SIF and GPP primarily result from a shared dependence on absorbed radiation or APAR
468 (Wohlfahrt et al., 2018; K. Yang et al., 2018), our findings also support many studies that have
469 demonstrated that GPP can be estimated from SIF observations from either satellite (Guanter et
470 al., 2012; Sun et al., 2017) or tower (Magney, Bowling, et al., 2019; Pierrat et al., 2022; X. Yang
471 et al., 2015). That the linear relationship between SIF and GPP is largely driven by APAR is
472 illustrated by stronger correlations between daily-averaged GPP with far-red SIF during spring
473 and fall months (Figure 4) when canopy changes drive large swings in fPAR. The strong
474 dependence of SIF on APAR also likely explains why correlations between far-red SIF and GPP
475 were stronger for weekly-averaged data (which are sensitive to seasonal light variability, but
476 average away changes driven by clouds and weather) than for daily-averaged data (which reflect
477 both seasonal and cloud/weather-driven variations in light; Figure 3). However, the decrease in
478 relative SIF values during the August 2018 drought (Figure 2a, c) demonstrate that SIF signals,
479 when normalized by light levels, may reflect changes in productivity that are independent from
480 APAR. This was confirmed by shared intraseasonal patterns between GPP/PAR, an LUE proxy,
481 and relative SIF (Figure 2c, d), and the strong correlation between detrended GPP/PAR and
482 relative red SIF during the August 2018 drought. These findings echo X. Yang et al. (2015) who

483 also showed that SIF provided information related to LUE above another temperate deciduous
484 location at Harvard Forest (US-Ha1).

485   We showed that SIF is more closely tied to APAR than to GPP at our site through the fact
486 that daily-averaged SIF data were more strongly correlated with downwelling PAR ($R^2 = 0.90$;
487 Figure 5a), which was roughly proportional to APAR during peak summer conditions with near-
488 constant NDVI, than it was with GPP ($R^2 = 0.61$; Figure 3b). Given that the correlation between
489 GPP and PAR was significantly weaker ($R^2 = 0.51$; Figure 5b), these results demonstrate the
490 challenges in using direct SIF observations to detect changes in LUE as they may not be an
491 effective indicator of synoptic-scale changes in productivity under mid-season conditions where
492 canopy structure and fPAR remain relatively stable. These results contrast with the findings of X.
493 Yang et al. (2015) who found only slightly weaker correlations between SIF and GPP than
494 between SIF and APAR at US-Ha1. US-Ha1 is, however, more radiation-limited than is US-
495 UMB (Wozniak et al., 2020), which would explain a closer coupling between variations in
496 radiation and GPP at their site. Our results are in line with those of K. Yang et al. (2018), who
497 found that SIF is a better indicator of APAR than of GPP albeit over a rice paddy. The different
498 relationships among SIF, GPP, and PAR in these three studies indicate that SIF-derived
499 estimates of productivity may not be free from the need for additional inputs, such as
500 meteorological conditions that may signal ecosystem stress (as have been used for NDVI-derived
501 estimates of GPP; see Running et al., 2004), but also that the necessity of these additional inputs
502 is likely influenced by whether ecosystem productivity is limited by water, temperature, or
503 radiation. At our site, we showed that relative far-red SIF responded to water stress and served as
504 a better proxy than SIF irradiances for seasonally detrended GPP during severe drought, however
505 this was only the case under water-limited conditions. Furthermore, as relative far-red SIF
506 tracked productivity only during drought conditions where SIF and PAR were decoupled from
507 GPP, we could not derive a simple regression model that combined absolute and relative SIF
508 observations to reflect both stressed and non-stressed conditions. Future studies should
509 investigate the necessity of using ancillary data or relative SIF to model GPP from space-based
510 SIF observations across ecosystems comprised of various plant types and also characterized by
511 various productivity limiting factors.

512   4.2 Relationship between SIF and Ecosystem Productivity

513   One key finding from this study is the variable relationship between far-red SIF and GPP
514 over the course of the growing season, with the linear slope between 90-minute far-red SIF and
515 GPP decreasing over the course of the growing season (Figure 4a). While a seasonally changing
516 relationship between SIF and productivity has been noted in previous studies (e.g. K. Yang et al.,
517 2018), these studies occurred over cropland where such changes could be attributed to structural
518 changes among different phenological stages. While we see the most drastic changes in spring
519 when there is rapid structural change, we show that the SIF:GPP relationship above a temperate
520 deciduous forest continues to evolve after the emergence of a well-developed canopy when
521 changes in canopy structure are minimal. The higher SIF:GPP slope in spring suggests that
522 assuming constant proportionality may lead to an overestimate of productivity in springtime, or
523 an underestimate in fall, when converting SIF to GPP based on an annual mean slope. Butterfield
524 et al. (2020) showed that interannual variability in satellite-based SIF observations is higher in
525 spring and is in better agreement with optical vegetation indices, whereas IAV in fall SIF is
526 small and only weakly correlated with other remote sensing products. The seasonal decline in the

527   SIF:GPP relationship could partly explain this phenomenon since it suggests that late-season
528   observations are characterized by a lower signal (and thus a lower signal-to-noise ratio) than are
529   spring data, potentially obscuring IAV. The decrease in the SIF:GPP slope as the growing season
530   progresses (Figure 4a) may be due to leaf age effects that impart subtle changes in the canopy.
531   Specifically, if leaves wilt or shrivel as they age due to progressive water stress, absorption of
532   PAR may shift slightly deeper into the canopy where f_{esc} is lower, thus leading to lower top-of-
533   canopy SIF. In the future, observations of leaf area and angle distribution over the course of the
534   growing season, in combination with canopy radiative transfer modeling, may help to further
535   elucidate the drivers of seasonal changes in the SIF:GPP slope.

536   The challenges of using SIF to estimate productivity under stable canopy conditions were
537   further illustrated by the limited response of red or far-red SIF irradiances to summer declines in
538   GPP. When GPP declined in response to drought conditions in August 2018, SIF signals
539   continued to reflect changes in radiation. Wohlfahrt et al. (2018) similarly found that SIF signals
540   in a Mediterranean pine forest exhibited poor correlation with GPP during a heat wave, although
541   their data indicated that that top-of-canopy SIF signals eventually declined in response to losses
542   in productivity. Marrs et al. (2020) also found that SIF signals in individual deciduous species
543   did not exhibit an immediate response to induced water stress. Yet, we found that relative far-red
544   SIF tracks stress-induced changes in GPP more effectively than SIF irradiances and various
545   vegetation indices over both daily and 5-day timescales, and that relative red SIF consistently
546   mirrored synoptic-scale changes in GPP/PAR, indicating that SIF observations do capture
547   changes in GPP and LUE when isolated from their dependence on PAR. While PAR levels in
548   Wohlfahrt et al. (2018) were largely consistent from day to day, indicating that SIF irradiances
549   should have been roughly proportional to relative SIF, we note the differences in timescale
550   between our two studies (i.e., the heatwave in their study occurred over a period of 8 days while
551   our observations captured the effects of longer-term, cumulative drought stress).

552   4.3 Applications of the Red:Far-red SIF Ratio

553   Our results show that the red:far-red SIF ratio is sensitive to changes in downwelling
554   PAR as well as canopy structure at both seasonal and interannual scales. Similar to Magney,
555   Frankenberg, et al. (2019), we saw considerably higher red:far-red ratios during early spring
556   canopy development, and in late fall as canopy chlorophyll content dropped, and as lower leaf
557   area and decreased chlorophyll content lead to decreased reabsorption of red SIF by the canopy.
558   The red:far-red SIF ratio showed significant differences between 2018 and 2019, with 2018
559   ratios being slightly lower than in 2019. These year-to-year differences in the red:far-red SIF
560   ratio are very likely explained by 2018 having greater NDVI and LAI values (see section 3.2), in
561   turn leading to variations in the canopy escape ratio for red fluorescence on interannual
562   timescales. However, we also showed that the red:far-red SIF ratio is highly correlated with
563   downwelling PAR (Figure 6c), suggesting that it is also dependent on light conditions that are
564   independent of canopy traits. These results highlight the value in simultaneous retrievals of SIF
565   at multiple wavelengths, which are becoming increasingly available from satellites such as
566   TROPOMI (Köhler et al., 2020), but also demonstrate that the interpretation of SIF observations

567   at multiple wavelengths must be cognizant of differences in sensitivity to ecosystem and
568   environmental changes on synoptic, seasonal, and interannual timescales.

569   Our results highlight the difficulty in leveraging the red:far-red SIF ratio to detect
570   ecosystem stress. Magney, Frankenberg, et al. (2019) showed that stressed conditions lead to a
571   lower red:far-red ratio at the leaf level, but that these leaf-level changes in NPQ were not
572   noticeable in canopy-level measurements. In contrast, Wohlfahrt et al. (2018) observed an
573   increase in the red:far-red ratio coinciding with a heat wave, and hypothesized that the
574   contrasting response of SIF at different wavelengths may have been due to a decrease in
575   chlorophyll content leading to less reabsorption of red fluorescence. Our results generally
576   corroborated Magney, Frankenberg, et al. (2019; see their Figure 7b, our Figure S6), and showed
577   that while the red:far-red SIF ratio at canopy-scale does reflect seasonal and interannual changes
578   in canopy structure, it is also influenced by changes in downwelling PAR (Figure 6c). Thus,
579   further studies into the response of the red:far-red SIF ratio to environmental stress would require
580   a detailed analysis of both the influence of phenological changes in canopy structure as well as
581   incoming light conditions on top-of-canopy SIF observations. These analyses necessitate that
582   observations be made at high temporal frequency since year-to-year or even month-to-month
583   changes are primarily driven by changes in canopy structure that are independent from
584   environmental stress, as well as the incorporation of canopy radiative transfer modeling.

585   **5 Conclusions**

586   We deployed a PhotoSpec system with two high spectral resolution spectrometers to measure red
587   and far-red SIF to a deciduous forest in northern Michigan. Results from the first two years of
588   data acquisition showed that SIF signals over a temperate deciduous forest are more strongly
589   related to radiation than to photosynthetic productivity. While a shared dependence on PAR did
590   result in a significant correlation between SIF and GPP, the slope of this linear relationship
591   gradually decreased over the course of the growing season, indicating that temporal changes in
592   the far-red SIF:GPP ratio should be considered when using SIF to assess ecosystem productivity.

593   Our study demonstrates challenges in using SIF irradiances to detect short-term stress-induced
594   declines in ecosystem productivity. Nonetheless, we show that observations of relative SIF may
595   be a more reliable indicator of ecosystem stress, indicating that SIF signals do respond to stress-
596   induced changes in productivity and track changes in LUE after accounting for changes in solar
597   radiation. Additionally, we show that the red:far-red SIF ratio is sensitive to seasonal and
598   interannual changes in canopy structure. Our results point to the need for coordinated multi-scale
599   studies on the relationship between SIF and photosynthesis including at the leaf and canopy
600   level, especially under conditions of environmental stress.

608 **Open Research**

609 SIF and other PhotoSpec data are available at https://doi.org/10.7302/sx8c-y281. AmeriFlux
610 environmental and eddy flux data are available at https://doi.org/10.17190/AMF/1246107.
611 OCO-2 SIF data are available at https://doi.org/10.5067/XO2LBBNPO010.
612

613 **References**

614 Aron, P. G., Poulsen, C. J., Fiorella, R. P., & Matheny, A. M. (2019). Stable Water Isotopes
615   Reveal Effects of Intermediate Disturbance and Canopy Structure on Forest Water
616   Cycling. Journal of Geophysical Research: Biogeosciences, 124(10), 2958–2975.
617

618 Beck, P. S. A., Atzberger, C., Høgda, K. A., Johansen, B., & Skidmore, A. K. (2006). Improved
619   monitoring of vegetation dynamics at very high latitudes: A new method using MODIS
620   NDVI. Remote Sensing of Environment, 100(3), 321–334.
621

622 Butterfield, Z., Buermann, W., & Keppel-Aleks, G. (2020). Satellite observations reveal seasonal
623   redistribution of northern ecosystem productivity in response to interannual climate
624   variability. Remote Sensing of Environment, 242, 111755.
625

626 Butterfield, Z., Muccio, D., Keppel-Aleks, G. (2022). Tower observations of solar-induced
627   chlorophyll fluorescence at the University of Michigan Biological Station, University of
628   Michigan - Deep Blue Data, (Dataset). https://doi.org/10.7302/sx8c-y281
629

630 Datt, B. (1999). A new reflectance index for remote sensing of chlorophyll content in higher
631   plants: Tests using Eucalyptus leaves. Journal of Plant Physiology, 154(1), 30–36.
632   https://doi.org/10.1016/S0176-1617(99)80314-9
633

634 Dechant, B., Ryu, Y., Badgley, G., Zeng, Y., Berry, J. A., Zhang, Y., Goulas, Y., Li, Z., Zhang,
635   Q., & Kang, M. (2020). Canopy structure explains the relationship between
636   photosynthesis and sun-induced chlorophyll fluorescence in crops. Remote Sensing of
637   Environment, 241, 111733.
638

639 Fotis, A. T., Morin, T. H., Fahey, R. T., Hardiman, B. S., Bohrer, G., & Curtis, P. S. (2018).
640   Forest structure in space and time: Biotic and abiotic determinants of canopy complexity
641   and their effects on net primary productivity. Agricultural and Forest Meteorology, 250,
642   181–191.
643

644 Frankenberg, C., Butz, A., & Toon, G. C. (2011). Disentangling chlorophyll fluorescence from
645   atmospheric scattering effects in O2 A-band spectra of reflected sun-light. Geophysical
646   Research Letters, 38(3).
647

648 Frankenberg, C., Fisher, J. B., Worden, J., Badgley, G., Saatchi, S. S., Lee, J., Toon, G. C., Butz,
649   A., Jung, M., & Kuze, A. (2011). New global observations of the terrestrial carbon cycle

from GOSAT: Patterns of plant fluorescence with gross primary productivity. Geophysical Research Letters, 38(17).

Frankenberg, C., O'Dell, C., Berry, J., Guanter, L., Joiner, J., Köhler, P., Pollock, R., & Taylor, T. E. (2014). Prospects for chlorophyll fluorescence remote sensing from the Orbiting Carbon Observatory-2. Remote Sensing of Environment, 147, 1–12.

Frasson, R. P. de M., Bohrer, G., Medvigy, D., Matheny, A. M., Morin, T. H., Vogel, C. S., Gough, C. M., Maurer, K. D., & Curtis, P. S. (2015). Modeling forest carbon cycle response to tree mortality: effects of plant functional type and disturbance intensity. Journal of Geophysical Research: Biogeosciences, 120(11), 2178–2193.

Friedlingstein, P., Jones, M. W., O'Sullivan, M., Andrew, R. M., Bakker, D. C. E., Hauck, J., le Quéré, C., Peters, G. P., Peters, W., & Pongratz, J. (2022). Global carbon budget 2021. Earth System Science Data, 14(4), 1917–2005.

Gamon, J. A., Field, C. B., Fredeen, A. L., & Thayer, S. (2001). Assessing photosynthetic downregulation in sunflower stands with an optically-based model. Photosynthesis Research, 67(1–2), 113–125.

Gitelson, A. A., & Gamon, J. A. (2015). The need for a common basis for defining light-use efficiency: Implications for productivity estimation. Remote Sensing of Environment, 156, 196–201.

Gough, C. M., Bohrer, G., & Curtis, P. (2022). AmeriFlux BASE US-UMB Univ. of Mich. Biological Station, Ver. 18-5. AmeriFlux AMP, (Dataset). https://doi.org/10.17190/AMF/1246107

Gough, C. M., Hardiman, B. S., Nave, L. E., Bohrer, G., Maurer, K. D., Vogel, C. S., Nadelhoffer, K. J., & Curtis, P. S. (2013). Sustained carbon uptake and storage following moderate disturbance in a Great Lakes forest. Ecological Applications, 23(5), 1202–1215.

Grossmann, K., Frankenberg, C., Magney, T. S., Hurlock, S. C., Seibt, U., & Stutz, J. (2018). Remote Sensing of Environment PhotoSpec : A new instrument to measure spatially distributed red and far- red Solar-Induced Chlorophyll Fluorescence. Remote Sensing of Environment, 216(June), 311–327. https://doi.org/10.1016/j.rse.2018.07.002

Guanter, L., Frankenberg, C., Dudhia, A., Lewis, P. E., Gómez-Dans, J., Kuze, A., Suto, H., & Grainger, R. G. (2012). Retrieval and global assessment of terrestrial chlorophyll fluorescence from GOSAT space measurements. Remote Sensing of Environment, 121, 236–251.

He, L., Ivanov, V. Y., Bohrer, G., Maurer, K. D., Vogel, C. S., & Moghaddam, M. (2014). Effects of fine-scale soil moisture and canopy heterogeneity on energy and water fluxes in a northern temperate mixed forest. Agricultural and Forest Meteorology, 184, 243–256.

Joiner, J., Guanter, L., Lindstrot, R., Voigt, M., Vasilkov, A. P., Middleton, E. M., Huemmrich, K. F., Yoshida, Y., & Frankenberg, C. (2013). Global monitoring of terrestrial chlorophyll fluorescence from moderate-spectral-resolution near-infrared satellite measurements: methodology, simulations, and application to GOME-2. Atmospheric Measurement Techniques, 6(10), 2803–2823.

Köcher, P., Gebauer, T., Horna, V., & Leuschner, C. (2009). Leaf water status and stem xylem flux in relation to soil drought in five temperate broad-leaved tree species with contrasting water use strategies. Annals of Forest Science, 66(1), 1.

Köhler, P., Behrenfeld, M. J., Landgraf, J., Joiner, J., Magney, T. S., & Frankenberg, C. (2020). Global Retrievals of Solar-Induced Chlorophyll Fluorescence at Red Wavelengths With TROPOMI. Geophysical Research Letters, 47(15), e2020GL087541.

Köhler, P., Frankenberg, C., Magney, T. S., Guanter, L., Joiner, J., & Landgraf, J. (2018). Global Retrievals of Solar-Induced Chlorophyll Fluorescence With TROPOMI: First Results and Intersensor Comparison to OCO-2. Geophysical Research Letters, 45(19), 10–456.

Lascano, R., Sojka, R. E., & Evett, S. (2007). Soil Water and Monitoring Technology. https://doi.org/10.2134/agronmonogr30.2ed.c2

Lasslop, G., Reichstein, M., Papale, D., Richardson, A. D., Arneth, A., Barr, A., Stoy, P., & Wohlfahrt, G. (2010). Separation of net ecosystem exchange into assimilation and respiration using a light response curve approach: critical issues and global evaluation. Global Change Biology, 16(1), 187–208.

le Quéré, C., Andrew, R. M., Friedlingstein, P., Sitch, S., Pongratz, J., Manning, A. C., Korsbakken, J. I., Peters, G. P., Canadell, J. G., Jackson, R. B., Boden, T. A., Tans, P. P., Andrews, O. D., Arora, V. K., Bakker, D. C. E., Barbero, L., Becker, M., Betts, R. A., Bopp, L., … Zhu, D. (2018). Global Carbon Budget 2017. Earth Syst. Sci. Data, 10, 405–448. https://doi.org/10.5194/essd-10-405-2018

Li, X., Xiao, J., Kimball, J. S., Reichle, R. H., Scott, R. L., Litvak, M. E., Bohrer, G., & Frankenberg, C. (2020). Synergistic use of SMAP and OCO-2 data in assessing the responses of ecosystem productivity to the 2018 US drought. Remote Sensing of Environment, 251, 112062.

Magney, T. S., Barnes, M. L., & Yang, X. (2020). On the covariation of chlorophyll fluorescence and photosynthesis across scales. Geophysical Research Letters, 47(23), e2020GL091098.

Magney, T. S., Bowling, D. R., Logan, B. A., Grossmann, K., Stutz, J., Blanken, P. D., Burns, S. P., Cheng, R., Garcia, M. A., & Köhler, P. (2019). Mechanistic evidence for tracking the seasonality of photosynthesis with solar-induced fluorescence. Proceedings of the National Academy of Sciences, 116(24), 11640–11645.

Magney, T. S., Frankenberg, C., Köhler, P., North, G., Davis, T. S., Dold, C., Dutta, D., Fisher, J. B., Grossmann, K., & Harrington, A. (2019). Disentangling changes in the spectral shape of chlorophyll fluorescence: Implications for remote sensing of photosynthesis. Journal of Geophysical Research: Biogeosciences, 124(6), 1491–1507.

Marrs, J. K., Reblin, J. S., Logan, B. A., Allen, D. W., Reinmann, A. B., Bombard, D. M., Tabachnik, D., & Hutyra, L. R. (2020). Solar-Induced Fluorescence Does Not Track Photosynthetic Carbon Assimilation Following Induced Stomatal Closure. Geophysical Research Letters, 47(15), e2020GL087956.

Matheny, A. M., Bohrer, G., Vogel, C. S., Morin, T. H., He, L., Frasson, R. P. de M., Mirfenderesgi, G., Schäfer, K. V. R., Gough, C. M., & Ivanov, V. Y. (2014). Species-specific transpiration responses to intermediate disturbance in a northern hardwood forest. Journal of Geophysical Research: Biogeosciences, 119(12), 2292–2311.

Matheny, A. M., Fiorella, R. P., Bohrer, G., Poulsen, C. J., Morin, T. H., Wunderlich, A., Vogel, C. S., & Curtis, P. S. (2017). Contrasting strategies of hydraulic control in two codominant temperate tree species. Ecohydrology, 10(3), e1815.

Miao, G., Guan, K., Yang, X., Bernacchi, C. J., Berry, J. A., DeLucia, E. H., Wu, J., Moore, C. E., Meacham, K., & Cai, Y. (2018). Sun-induced chlorophyll fluorescence, photosynthesis, and light use efficiency of a soybean field from seasonally continuous measurements. Journal of Geophysical Research: Biogeosciences, 123(2), 610–623.

Monteith, J. L. (1977). Climate and the efficiency of crop production in Britain. Philosophical Transactions of the Royal Society of London. B, Biological Sciences, 281(980), 277–294.

Morin, T. H., Bohrer, G., Frasson, R. P. d M., Naor-Azreli, L., Mesi, S., Stefanik, K. C., & Schäfer, K. V. R. (2014). Environmental drivers of methane fluxes from an urban temperate wetland park. Journal of Geophysical Research: Biogeosciences, 119(11), 2188–2208.

Pierrat, Z., Magney, T., Parazoo, N. C., Grossmann, K., Bowling, D. R., Seibt, U., Johnson, B., Helgason, W., Barr, A., & Bortnik, J. (2022). Diurnal and Seasonal Dynamics of Solar-Induced Chlorophyll Fluorescence, Vegetation Indices, and Gross Primary Productivity in the Boreal Forest. Journal of Geophysical Research: Biogeosciences, 127(2), e2021JG006588.

Rebmann, C., Kolle, O., Heinesch, B., Queck, R., Ibrom, A., & Aubinet, M. (2012). Data acquisition and flux calculations. In Eddy covariance (pp. 59–83). Springer.

Reichstein, M., Falge, E., Baldocchi, D., Papale, D., Aubinet, M., Berbigier, P., Bernhofer, C., Buchmann, N., Gilmanov, T., & Granier, A. (2005). On the separation of net ecosystem exchange into assimilation and ecosystem respiration: review and improved algorithm. Global Change Biology, 11(9), 1424–1439.

Running, S. W., Nemani, R. R., Heinsch, F. A., Zhao, M., Reeves, M., & Hashimoto, H. (2004). A continuous satellite-derived measure of global terrestrial primary production. AIBS Bulletin, 54(6), 547–560.

Ryu, Y., Berry, J. A., & Baldocchi, D. D. (2019). What is global photosynthesis? History, uncertainties and opportunities. Remote Sensing of Environment, 223, 95–114.

Science Team, O.-2, Gunson, M., & Eldering, A. (2017). OCO-2 Level 2 bias-corrected solar-induced fluorescence and other select fields from the IMAP-DOAS algorithm aggregated as daily files, Retrospective processing V8r. Goddard Earth Sciences Data and Information Services Center (GES DISC). 10.5067/AJMZO5O3TGUR

Song, L., Guanter, L., Guan, K., You, L., Huete, A., Ju, W., & Zhang, Y. (2018). Satellite sun-induced chlorophyll fluorescence detects early response of winter wheat to heat stress in the Indian Indo-Gangetic Plains. Global Change Biology, 24(9), 4023–4037.

Sun, Y., Frankenberg, C., Jung, M., Joiner, J., Guanter, L., Köhler, P., & Magney, T. (2018). Overview of Solar-Induced chlorophyll Fluorescence (SIF) from the Orbiting Carbon Observatory-2: Retrieval, cross-mission comparison, and global monitoring for GPP. Remote Sensing of Environment, 209, 808–823.

Sun, Y., Frankenberg, C., Wood, J. D., Schimel, D. S., Jung, M., Guanter, L., Drewry, D. T., Verma, M., Porcar-Castell, A., & Griffis, T. J. (2017). OCO-2 advances photosynthesis observation from space via solar-induced chlorophyll fluorescence. Science, 358(6360), eaam5747.

Svoboda, M., LeComte, D., Hayes, M., Heim, R., Gleason, K., Angel, J., Rippey, B., Tinker, R., Palecki, M., & Stooksbury, D. (2002). The drought monitor. Bulletin of the American Meteorological Society, 83(8), 1181–1190.

Tucker, C. J. (1979). Red and photographic infrared linear combinations for monitoring vegetation. Remote Sensing of Environment, 8(2), 127–150. https://doi.org/https://doi.org/10.1016/0034-4257(79)90013-0

Wohlfahrt, G., Gerdel, K., Migliavacca, M., Rotenberg, E., Tatarinov, F., Müller, J., Hammerle, A., Julitta, T., Spielmann, F. M., & Yakir, D. (2018). Sun-induced fluorescence and gross primary productivity during a heat wave. Scientific Reports, 8(1), 14169.

Wolanin, A., Rozanov, V. v, Dinter, T., Noël, S., Vountas, M., Burrows, J. P., & Bracher, A. (2015). Global retrieval of marine and terrestrial chlorophyll fluorescence at its red peak using hyperspectral top of atmosphere radiance measurements: Feasibility study and first results. Remote Sensing of Environment, 166, 243–261.

Wozniak, M. C., Bonan, G. B., Keppel-Aleks, G., & Steiner, A. L. (2020). Influence of Vertical Heterogeneities in the Canopy Microenvironment on Interannual Variability of Carbon

Uptake in Temperate Deciduous Forests. Journal of Geophysical Research: Biogeosciences, 125(8), e2020JG005658.

Yang, K., Ryu, Y., Dechant, B., Berry, J. A., Hwang, Y., Jiang, C., Kang, M., Kim, J., Kimm, H., & Kornfeld, A. (2018). Sun-induced chlorophyll fluorescence is more strongly related to absorbed light than to photosynthesis at half-hourly resolution in a rice paddy. Remote Sensing of Environment, 216, 658–673.

Yang, X., Tang, J., Mustard, J. F., Lee, J., Rossini, M., Joiner, J., Munger, J. W., Kornfeld, A., & Richardson, A. D. (2015). Solar-induced chlorophyll fluorescence that correlates with canopy photosynthesis on diurnal and seasonal scales in a temperate deciduous forest. Geophysical Research Letters, 42(8), 2977–2987.

Yazbeck, T., Bohrer, G., Gentine, P., Ye, L., Arriga, N., Bernhofer, C., Blanken, P. D., Desai, A. R., Durden, D., & Knohl, A. (2021). Site Characteristics Mediate the Relationship Between Forest Productivity and Satellite Measured Solar Induced Fluorescence. Frontiers in Forests and Global Change, 193.

Yoshida, Y., Joiner, J., Tucker, C., Berry, J., Lee, J.-E., Walker, G., Reichle, R., Koster, R., Lyapustin, A., & Wang, Y. (2015). The 2010 Russian drought impact on satellite measurements of solar-induced chlorophyll fluorescence: Insights from modeling and comparisons with parameters derived from satellite reflectances. Remote Sensing of Environment, 166, 163–177.

Yu, L., Wen, J., Chang, C. Y., Frankenberg, C., & Sun, Y. (2019). High-resolution global contiguous SIF of OCO-2. Geophysical Research Letters, 46(3), 1449–1458.

Zeng, Y., Badgley, G., Dechant, B., Ryu, Y., Chen, M., & Berry, J. A. (2019). A practical approach for estimating the escape ratio of near-infrared solar-induced chlorophyll fluorescence. Remote Sensing of Environment, 232, 111209.